Mg2+, Sr2+, Ag+, and Cu2+ co-doped beta-tricalcium phosphate: Improved thermal stability and mechanical and biological properties

Nicolas Somers, Florian Jean, Marie Lasgorceix, Giovanni Urruth, Sandra Balvay, Claire Gaillard, Laurent Gremillard, Anne Leriche

Mg2+, Sr2+, Ag+, and Cu2+ co-doped β-tricalcium phosphate: Improved thermal stability and mechanical and biological properties

This article has been published in
Journal of the American Ceramic Society (2023) Vol. 106. , issue 7, pp. 4061-75
https://doi.org/10.1111/jace.19093

Nicolas Somers [a,*], Florian Jean [a], Marie Lasgorceix [a], Giovanni Urruth [b], Sandra Balvay [c], Claire Gaillard [c], Laurent Gremillard [c], Anne Leriche [a]

[a] Univ Polytechnique Hauts-De-France – CERAMATHS-DMP, F-59313 Valenciennes, France
[b] CIRIMAT, Université de Toulouse, CNRS, France
[c] Univ Lyon, CNRS, INSA Lyon, UCBL, MATEIS, UMR5510, 69100 Villeurbanne, France

* Corresponding author: nicolas.somers@alumni.uliege.be

Abstract

β-tricalcium phosphate (β-TCP, β-$Ca_3(PO_4)_2$) is an attractive biomaterial for bone repair applications. However, its sintering and mechanical properties are limited by a problematic phase transition to α-TCP. Cationic doping of β-TCP is able to postpone the formation of α-TCP allowing higher sintering temperatures and better mechanical properties. The co-doping of β-TCP with Mg^{2+} and Sr^{2+} has already been studied in detail, but the addition of antibacterial cations (Ag^{+} and Cu^{2+}) on the Mg–Sr β-TCP co-doped composition remains unexplored. Thus, two co-doped β-TCP compositions were realized by aqueous precipitation technique without any secondary phase and compared with undoped β-TCP: Mg–Sr (2.0–2.0 mol%) and Mg–Sr–Ag–Cu (2.0–2.0–0.1–0.1 mol%). Differential thermal analysis and dilatometry analyses showed a slight decrease of the β-TCP → α-TCP phase transition temperature for the Mg–Sr–Ag–Cu (2.0–2.0–0.1–0.1% mol) composition as compared to the Mg–Sr (2.0–2.0 mol%). However, both exhibited much higher transition temperatures than undoped β-TCP. The addition of Ag^{+} and Cu^{2+} slightly reduces the grain size after sintering compared to the Mg–Sr (2.0–2.0 mol%) and the undoped compositions. The co-doped compositions also exhibited improved mechanical properties, specifically a higher Vickers hardness and elastic modulus. Finally, cell proliferation assays showed that the presence of dopants, even Ag^{+} and Cu^{2+}, does not affect the survival and proliferation of cells. Thus, the use of Mg^{2+}, Sr^{2+}, Ag^{+}, and Cu^{2+} co-doped β-TCP could be very promising for biomedical applications due to the improvements of these dopants on the thermal stability and mechanical and biological properties.

Keywords:

β-TCP; Doping; Magnesium; Strontium; Silver; Copper; Coprecipitation synthesis; Sintering; Hardness; Cytocompatibility; Cell proliferation; Bone repair applications.

1. Introduction

Bone remodelling is a continuous process in a human's life and is essential to maintain the main functions of bone tissues. Above all, this process is essential to heal any damage inflicted on the bones. Bone remodelling can vary over time and is faster in childhood, slowing down sharply with age.[1-5] However, sometimes, this self-healing mechanism is not sufficient to repair a fracture or damage caused by disease (osteonecrosis or bone cancer) or reconstructive surgery. In these cases, surgical procedures involving the removal of the damaged bone are necessary and can cause significant loss of bone mass that bone remodelling cannot replace.[6, 7] The reconstruction of the bone must then be assisted with the help of a bone graft. Currently, the most used type of bone graft is the autograft that involves harvesting a bone fraction from the patient's body and then grafting it at the damaged site. Despite providing natural bone cells and growth factors, autografts present some important drawbacks like limited quantities and heavy surgical procedures with two operation sites (harvesting and grafting).[8, 9] In order to solve the issues associated with autografts, researchers are looking into the production of synthetic bone substitutes (alloplastic grafts) that should ideally exhibit properties similar to natural bone.[6, 7, 10]

Among the different materials available to produce alloplastic grafts, β-tricalcium phosphate (β-TCP, β-$Ca_3(PO_4)_2$) is an attractive biomaterial for bone repair applications due to its biocompatibility, bioactivity, and bioresorbability. Indeed, this material could be gradually degraded after grafting and replaced by new bones after some months. For these reasons, β-TCP is already used in the bone grafting market (BIOSORB, CALCIRESORB, CEROS, CERASORB, RTR, VITOSS, OSFERION, CHRONOS, and so on) in the form of granules, cements, or macroporous scaffolds.[11-14] The realization of macroporous scaffolds is challenging because the introduction of porosity, necessary to create a favourable osteogenic environment, reduces the mechanical properties.[8,15] This reduction of mechanical properties, also linked to the β-TCP ability to be sintered, is one of the main challenges to extend the use of β-TCP porous scaffolds as well as their inconsistent biological behaviour with conflicting clinical results.[11,15] According to Bohner *et al.*,[11] β-TCP sintering efficiency is limited for two main reasons: the presence of impurities and the β to α-TCP phase transition. The first one could be solved by a perfect control of the powder stoichiometry during the synthesis.[13,16,17] The phase transition is more problematic because it occurs at a relatively low temperature (1115–1200°C), which is detrimental to the achievement of high densities.[18] Above all, this transition is characterized by a ∼7% increase in volume. This leads to crack formation thereby limiting the sintering and the final mechanical properties of the ceramic parts.[11,13,17]

Among the available solutions in the literature to optimize the densification of β-TCP, one seems particularly interesting: cationic doping. Indeed, some cations are able to stabilize the β-TCP phase and postpone the formation of α-TCP allowing higher temperature sintering.[11,13,19-24] Among all the possible dopants, magnesium and strontium already showed interesting properties like an improvement of densification, thermal stability, and mechanical properties of β-TCP.[19,24-32] Indeed, it has been shown that Mg^{2+} and Sr^{2+} dopings and co-dopings postpone the β → α transition, and a higher densification rate was observed compared to undoped β-TCP.[25,26,32] An improved densification can lead to better mechanical properties. The compressive strength of commercial β-TCP rectangular blocks (OSferion) examined by Yamasaki et al.[33] reaches 2.93 MPa, whereas Tarafder et al.[21] were able to reach up to 9 MPa for scaffolds made with Sr^{2+}–Mg^{2+}-doped β-TCP. Thus, co-doped Sr^{2+}–Mg^{2+} β-TCP seems very promising for the manufacture of improved β-TCP scaffolds. For this reason, a previous work of the authors was focused on synthetizing eight different compositions of doped β-TCP with magnesium and strontium and studying the effect on the thermal stability and densification of β-TCP.[25]

In addition to modulating the physical features of β-TCP, the incorporation of metal ions can improve the osteoinductive capacity of β-TCP scaffolds. For example, Zhang et al.[34] demonstrated that the application of Cu^{2+} could enhance the osteogenic and angiogenic capacities of β-TCP powders. The release of metal ions can improve the biological performance of bone regenerative scaffolds as well as give antibacterial properties to limit the risk of infection with synthetic bone grafting.[22,35,36]

The improvement of β-TCP both mechanical and biological properties as well as providing an antibacterial activity would give new perspectives for the use of β-TCP scaffolds for bone repair applications. In this framework, the focus of this work is to study the impact of antibacterial cations (Ag^{+} and Cu^{2+}) on the Mg–Sr β-TCP co-doped composition. Silver and copper ions are known to possess antimicrobial and antibacterial properties that could be beneficial to limit postoperative infections.[37]

Gokcekaya et al. clearly showed that silver doping of β-TCP stabilizes the β phase, and the formation of α-TCP is limited when the silver content increases.[38] According to Liu et al., the incorporation of silver in the structure would not modify the crystallization properties of β-TCP nor its mechanical properties, only bringing a bactericidal activity.[39] For copper doping, Fadeeva et al. and Cummings et al. showed that the introduction of Cu prevented the polymorphic transformation of β- to α-TCP, whereas enhanced the crystal growth and porosity of the ceramics, which had a positive effect on the cytocompatibility of the material.[40,41] Despite the cited research on silver and copper doping of β-TCP, few data are available concerning their role on the sintering and mechanical properties. The co-doping of β-TCP with Mg^{2+} and Sr^{2+} has already been studied in detail, but the addition of antibacterial cations (Ag^{+} and Cu^{2+}) on the Mg–Sr β-TCP co-doped composition remains unexplored. The associations of antibacterial cations with cations proven effective for mechanical properties (Mg^{2+} and Sr^{2+}) have never been studied.

For these reasons, Mg^{2+}, Sr^{2+}, Ag^{+}, and Cu^{2}+ co-doped β-TCP has been synthesized in this work. The compositions of the produced powders as well as their thermal stability were assessed. The effects of the dopants on the densification and mechanical properties of β-TCP were also evaluated. Finally, cell proliferation assays were conducted to figure out the biocompatibility of the co-doped composition involving magnesium, strontium, silver, and copper.

2. Materials and methods

2.1 Synthesis of doped β-TCP powders

β-TCP powders were produced following the process described in our previous works[25] with the addition of magnesium, strontium, silver, and copper cations as nitrates, $Mg(NO_3)_2$ (98.0%–102.0%, MW 256.41, Alfa Aesar, Germany), $Sr(NO_3)_2$ (>99%, MW 211.63, Carlo Erba, France), $Ag(NO_3)$ (>99%, FW 169.88, Alfa Aesar, Germany), and $Cu(NO_3)_2{\cdot}5H_2O$ (98.0%–102.0%, FW 232.59, Alfa Aesar, Germany) into the calcium nitrate solution. The pH was fixed at 7.2, and the stoichiometric amount of calcium was reduced to allow dopant substitutions, but the ratio (Ca + dopant)/P was kept at 1.5 corresponding to stoichiometric β-TCP. The temperature was fixed at 31°C during all the syntheses. At the end of the ripening time of 20 h, the apatitic tricalcium phosphate precipitate was extracted, filtered, and washed with 500 mL of DI water. The precipitate was dried at 70°C for 24 h before calcination at 850°C for 3 h. The heating rate was fixed at 180°C/h, whereas the cooling rate was 200°C/h.

The synthesis of M-doped β-TCP (where M can be magnesium, strontium, or copper) is reported as an example in the following equations:

$$(9-x)Ca(NO_3)_2 + 6(NH_4)_2HPO_4 + 6NH_4OH + xM(NO_3)_2 \xrightarrow{31°C} Ca_{9-x}M_x(HPO_4)(PO_4)_5(OH) + 18NH_4NO_3 + 5H_2O \quad (1)$$

$$Ca_{9-x}M_x(HPO_4)(PO_4)_5(OH) \xrightarrow{>700°C} 3\left(Ca_{3-\frac{x}{3}}M_{\frac{x}{3}}\right)(PO_4)_2 + H_2O \quad (2)$$

The synthesis of Ag-doped β-TCP is reported as an example in the following equations:

$$\left(9-\frac{x}{2}\right)Ca(NO_3)_2 + 6(NH_4)_2HPO_4 + 6NH_4OH + xAg(NO_3)_2 \xrightarrow{>31°C} Ca_{9-\frac{x}{2}}Ag_x(HPO_4)(PO_4)_5(OH) + 18NH_4NO_3 + 5H_2O \quad (3)$$

$$Ca_{9-\frac{x}{2}}Ag_x(HPO_4)(PO_4)_5(OH) \xrightarrow{>700°C} 3\left(Ca_{3-\frac{x}{6}}Ag_{\frac{x}{3}}\right)(PO_4)_2 + H_2O \quad (4)$$

Two co-doped compositions were realized: Mg–Sr (2.0–2.0 mol%) and Mg–Sr–Ag–Cu (2.0–2.0–0.1–0.1 mol%). Percentages are in function of the calcium content. Doping amounts of silver and copper were chosen according to previous works that showed cytotoxicity with amounts higher than 0.2% of Ag^{+}/Cu^{2+}.[41-43]

2.2 Shaping and sintering of doped β-TCP powders

After calcination, powders were ball milled at 100 rpm during 4 h in a high-density polyethylene (HDPE) milling jar with partially stabilized zirconia (Y-PSZ) grinding media balls. After milling, powders have optimal characteristics to be shaped into pellets.

The milled powders were then dried at 70°C for 24 h and shaped to 14 mm diameter pellets by mould casting. β-TCP slurries were prepared with a fixed powder concentration of 65 wt% in water with a commercial organic deflocculant (Darvan C, R.T. Vanderbilt Co.) introduced in the amount of 2 mg m^{-2} with respect to the powder surface area. After 1 h of ball milling in an HDPE milling jar with Y-PSZ grinding media balls, β-TCP slurries were poured into a 24-well cell culture plate and placed on a plasterboard. A period of 2 h after casting and when the majority of the water present has been absorbed by the plaster, the pellets are carefully removed from the culture plate and dried for 24 h at 40°C. The dried pellets are lightly polished with P1000 grade SiC sandpaper to remove excess material.

Pellets of the three compositions (undoped β-TCP as well as the co-dopings Mg–Sr [2.0–2.0 mol%] and Mg–Sr–Ag–Cu [2.0–2.0–0.1–0.1% mol]) were sintered by conventional route at 1100 and 1300°C with a dwell time of 3 h. The heating rate was fixed at 300°C/h, whereas the cooling rate was 200°C/h.

2.3 Characterization techniques

2.3.1 Physicochemical characterization of the powders

Purity of the raw material was assessed on powders calcined at 1000°C for 15 h just after drying according to the standard procedure NF ISO 13779-3:2008-04. This section of ISO 13779 specifies test methods for the chemical analysis and quantification of the crystallinity and foreign phases of calcium phosphate materials such as coatings and sintered products. The standard stipulates that calcium phosphate samples must first be calcined at 1000°C for 15 h before analysis. The detection of the hydroxyapatite ($Ca_{10}(PO_4)_6(OH)_2$, HA) phase was performed by powder X-ray diffraction (XRD) with the HA (2 1 1) (2θ = 31.772°) most intense diffraction peak. XRD patterns were recorded using a $\theta/2\theta$ diffractometer (Panalytical X'PERT PRO) working with Cu K_α radiation (1.541874 Å) at 45 kV and 40 mA; the measurement was carried out in the 2θ range of 10°–60°, with the step of 0.0066° and 78.795 s of acquisition time. The crystalline phases were identified using Joint Committee on Powder Diffraction-International Centre for Diffraction Data (JCPDS-ICDD) files. XRD measurements were also carried out on the surface of sintered pellets to investigate the presence of α-TCP. All the diffractograms were normalized with the most intense peak (31.027° (0 2 1 0)) of the β-TCP phase fixed at 100. Moreover, Rietveld refinement using the Profex software[44] was used to determine lattice parameters of the different compositions as well as for the quantification of potential secondary phases.

The detection of calcium pyrophosphate ($Ca_2P_2O_7$, CPP) was verified by infrared spectroscopy (IR) with its 720 and 1200 cm^{-1} characteristic bands because its most intense XRD usable peak (2 0 2) (2θ = 28.9°) is only observable for quantities higher than 4 wt%. Infrared spectra of powders were recorded on a Fourier transform spectrometer (JASCO FT/IR-460 Plus) in the 4000–400 cm^{-1} region with a resolution of 2 cm^{-1}. Each of the collected spectra is an average of 16 FTIR scans. For measurements, 0.01 g of β-TCP powder is mixed and ground manually with 3 g of potassium bromide KBr in an agate mortar.

Inductively coupled plasma–atomic emission spectroscopy (ICP–AES, using a Shimadzu ICPE-9820, 125–770 nm and ultrapure standards SCP Science PlasmaCAL) was used to check the purity and chemical composition of the synthesized powders. Standards and samples were dissolved in ultrapure nitric acid (70 vol%) and diluted in pure water (1, 20, 30, and 50 mg·L^{-1}). ICP–AES measurements also allow to determine the dopant(s)/(Ca + dopant(s)) molar ratios as well as the (Ca + dopant(s))/P ratios.

2.3.2 Thermal stability of co-doped β-TCP

The thermal behaviour of the produced powders was assessed by differential thermal analysis (DTA) and thermogravimetric analysis experiments using an LABSYS EVO (Setaram) equipment on uncalcined and dried powders with a sample weight of about 25 mg, heating rate 10°C·min^{-1} from 20 to 1500°C, and airflow 40 mL·min^{-1}.

The α-to-β phase transition of the TCP for the different compositions was characterized by dilatometric analyses on casted parallelepiped-shaped pellets using a Dil-402C (NETZSCH) dilatometer. Casted parallelepiped-shaped pellets were prepared in a manner similar to moulded pellets. After 1 h of ball milling, casting, and drying, pellets were shaped to parallelepiped by polishing with P1000 grade SiC sandpaper. Before analyses, pellets were pre-sintered at 1000°C for 12 h to observe the interruption of shrinkage and the dilatation associated with the α-TCP formation. Thermal expansion–shrinkage of these pellets was measured in air atmosphere. Measurements were performed up to 1500°C.

2.3.3 Characterization of sintered pellets

2.3.3.1 Relative densities

Relative densities (RDs) of sintered pellets were determined by the Archimedes principle in deionized water at room temperature using an immersion time of 2 h after 15 min of vacuum. The weighing process was conducted on an analytical balance with a resolution of 0.1 mg. A series of three samples per composition and temperature were analysed to obtain average RD values. Theoretical densities were obtained by the Rietveld refinement of diffractograms obtained for each composition (Profex).[25,44]

2.3.3.2 Microstructure

Sintered microstructures (1100°C, 3 h) were observed on pellet surfaces using scanning electron microscopy (SEM) (Hitachi SU5000, BSE 15.0 kV ×5.00k) after polishing and thermal etching. The polishing was carried out using SiC paper discs and diamond pastes (down to 0.5–3 μm), and the samples were heated at 950°C for 15 min for the thermal etching. Samples were fixed on SEM supports with conductive adhesive carbon tape, and a sputter coating with a gold target was applied for 1 min before SEM observation. Grain size measurements were carried out by image treatment (ImageJ) on 60 grains with 4 measurements by grain. The average grain sizes were multiplied by $4/\pi$ according to the Abercrombie relation to get the radius of a particle from any profile.[45]

2.3.3.3 Mechanical properties

Indentation tests were performed on casted, sintered (1100°C, 3 h), and polished pellets with a ZHU 0.2 instrumented Vickers indenter, Zwick Roell. A load of 2 N is applied for 15 s. These parameters were chosen according to previous works at the laboratory[16,46] and to the standard CSM test procedure in order to partially avoid the artefacts related to the creep and the filling of porosities as well as cracking.[47] A series of 30 indentations were made on each sample, and 3 samples were tested per composition.

2.3.4 Cytocompatibility evaluation and cell proliferation on sintered pellets

Preliminary evaluation of the co-doped β-TCP cytocompatibility was carried out on sintered pellets (1100°C, 3 h) using MG63 cells and human tumour cell lines (osteoblast line obtained from adult skin explants).

Once the ideal cell concentration has been reached (10 000 cells for 50 μL of suspension) after a series of dilutions with culture medium, 50 μL of suspension were taken, and cells were seeded onto sterile samples (oven at 180°C for 1 h) into 24-well cell culture plates (Corning, USA). After 2 h incubation in a humidified atmosphere (37°C, 5% CO_2, 95% humidity), 2 mL of complete medium was added to each well before placing the cell culture plate again in the incubator (37°C, 5% CO_2, 95% humidity) for 24 h. In parallel, cells were cultured over the bare bottom surface of the well to serve as control.

Cell proliferation tests on sintered pellets were carried out in a similar way than the cytocompatibility evaluation except that the ideal cell concentration was 5000 cells for 50 μL of suspension. Moreover, the cell culture plate was placed in the incubator (37°C, 5% CO_2, 95% humidity) for 3, 6, and 10 days. Culture medium was renewed every 3 days. These steps of cell seeding onto the samples are shown in Figure 1.

After 1, 3, 6, and 10 days in the incubator, cell viability was assessed by the resazurin test. Once all the supernatant is removed, the wells are rinsed twice with 2 mL of DMEM medium (without serum and phenol red). In parallel, a 10% PrestoBlue (Invitrogen) solution is prepared in DMEM without phenol red or serum. PrestoBlue is a cell-permeable resazurin solution for the quantitative measurement of cell viability. The prepared 10% Medium-PrestoBlue solution is added to each well containing samples (1 mL per well). The culture plate is then placed in the incubator for 1 h and 30 min (37°C, 5% CO_2, 95% humidity). After this period, the 24-well plate is slightly shaken to homogenize the media, and then, each well of 100 μL is transferred to a 96-well black bottom plate (Corning, USA). Black bottom plates are

used to measure the fluorescence of suspensions with an INFINITE PRO 200 reader (Tecan), an automated plate reader equipped with a spectrofluorometer. For these tests, fluorescence is read at the wavelengths of 535 nm (excitation) and 610 nm (emission). This test is repeated three times on three samples of each composition. The steps carried out for reading fluorescence with PrestoBlue are shown in Figure 2.

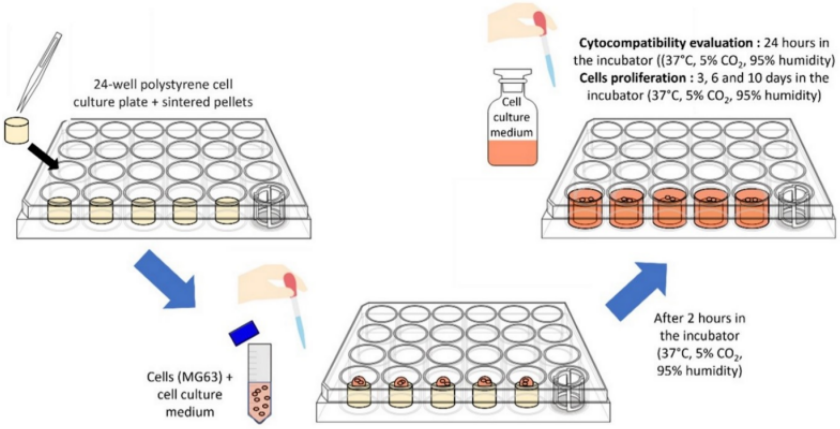

Figure 1. Procedure of cell seeding onto samples for cell proliferation tests.

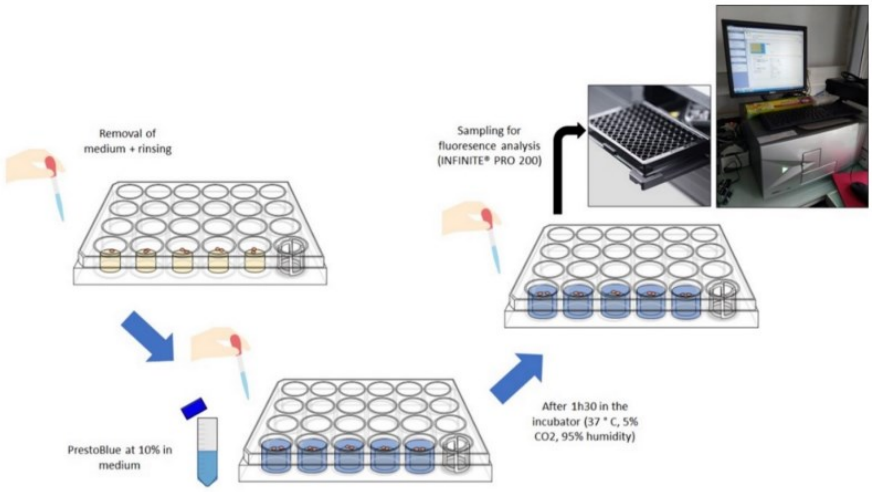

Figure 2. Resazurin (PrestoBlue) test procedure.

3. Results and discussion

3.1 Physicochemical characterization of the powders

XRD patterns of undoped and co-doped β-TCP powders after calcination for 15 h at 1000°C are shown in Figure 3. The absence of HA as well as CPP is visible for every composition, and all diffraction peaks correspond to the β-TCP phase. Moreover, the doped samples exhibit a small shift in peak position compared to the undoped β-TCP. The incorporation of the dopants in the β-TCP structure modifies the lattice volume and shifts the diffraction angles.[23-25,48]

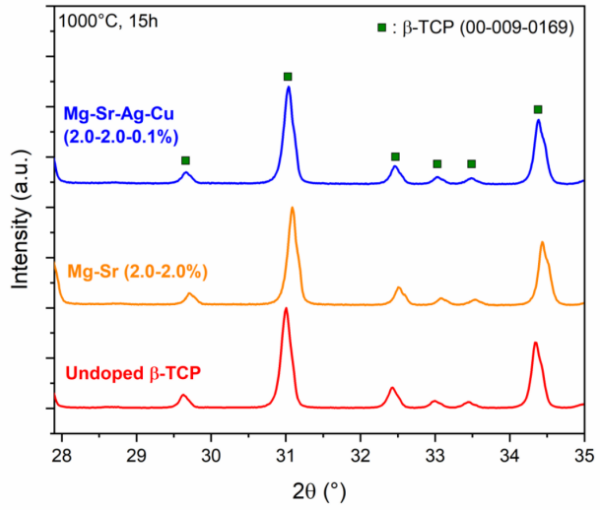

Figure 3. X-ray diffraction (XRD) patterns of undoped and co-doped β-TCP powders after calcination at 1000°C during 15 h.

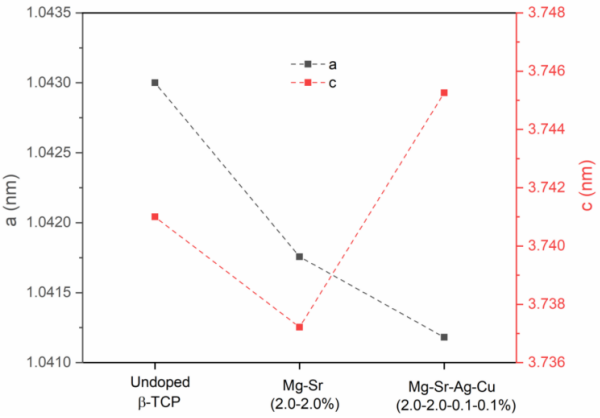

Figure 4. Lattice parameters (a- and c-axis) for undoped and co-doped β-TCP powders obtained by Rietveld refinement (Profex).

Rietveld refinements indicate the presence of 100% of β-TCP without any secondary phase. Figure 4 shows the changes in lattice parameters for the different compositions. The Mg–Sr (2.0–2.0 mol%) composition shows a global decrease of the unit cell parameters. According to Kannan et al.,[49] given the higher ionic radii of Sr^{2+} (1.25 Å) in comparison with Ca^{2+} (1.12 Å), the substitution of Ca^{2+} by Sr^{2+} should increase the size of the unit cell of β-TCP lattice. On the other hand, the co-substitution of lower sized Mg^{2+} (0.89 Å) for Ca^{2+} would reasonably tend to decrease the size of unit cell. However, the combined substitution of Sr^{2+} and Mg^{2+}, with their share of equal concentrations in the β-TCP structure, caused a reduction in the unit cell parameters. That is why a decrease in the unit cell parameters of β-TCP structure is observed, due to the fact that the average size of substituted Sr^{2+} and Mg^{2+} ions (1.25 + 0.89 Å)/2 = 1.07 Å is lower than the size of Ca^{2+} ion that has been replaced.[49] Concerning the Mg–Sr–Ag–Cu (2.0–2.0–0.1–0.1 mol%) composition, a decrease in the cell parameter *a* is observed where the *c* parameter increases suddenly compared to the Mg–Sr (2.0–2.0 mol%) composition. The decrease in the cell parameter *a* could be explained by the smaller ionic radius of Cu^{2+} ions (0.80 Å) compared to Ca^{2+} ions (1.12 Å), reducing the lattice volume with the substitution. On the other hand, the increase in the *c* parameter might come from the incorporation of the bigger ion Ag^{+} (1.15 Å), which stretches the lattice in the *c*-axis. Finally, these observed changes in lattice parameters confirm that the dopants have entered the β-TCP structure as predicted.

The IR analyses of undoped and co-doped compositions are shown in Figure 5. The absence of CPP characteristic bands (720 and 1200 cm^{-1}) is clearly visible for every composition. Thus, based on XRD and IR results, the developed synthesis process can obtain either undoped or co-doped β-TCP powders without any secondary phase.

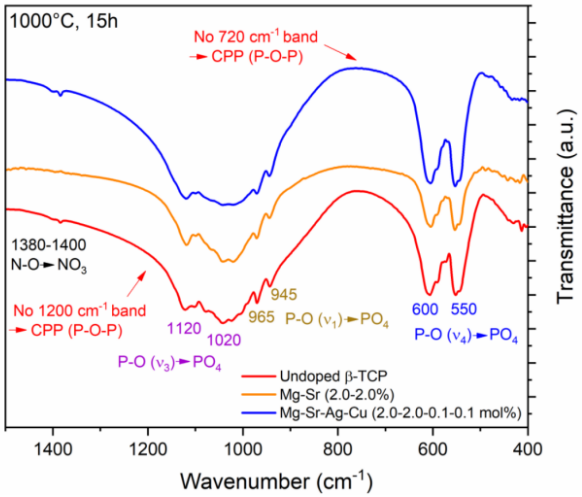

Figure 5. Infrared spectroscopy (IR) spectra of undoped and co-doped β-TCP powders after calcination at 1000°C during 15 h.

Incorporation of dopants was also assessed by ICP–AES analyses. Results of these analyses are shown in Table 1. The experimental dopant percentages (dopants/[Ca + dopants]) are close to the nominal ones, and the (Ca + dopant(s))/P atomic ratios are slightly larger than the stoichiometric 1.5 value for the Mg–Sr (2.0–2.0 mol%) composition.

Table 1. Chemical composition of the synthesized powders obtained by inductively coupled plasma–atomic emission spectroscopy (ICP–AES). The values are given with a relative error of 0.01%

Nominal composition Mg–Sr–Ag–Cu (mol%)	ICP–AES ratio Mg/(Ca + Mg + Sr + Ag + Cu) (mol%)	ICP–AES ratio Sr/(Ca + Mg + Sr + Ag + Cu) (mol%)	ICP–AES ratio Ag/(Ca + Mg + Sr + Ag + Cu) (mol%)	ICP–AES ratio Cu/(Ca + Mg + Sr + Ag + Cu) (mol%)	ICP–AES ratio (Ca + Mg + Sr + Cu)/P (molar ratio)
2.0–2.0	2.80	2.00	/	/	1.57
2.0–2.0–0.1–0.1	3.10	2.12	0.06	0.14	1.50

3.2 Thermal stability of co-doped β-TCP

Powder DTA curves of the different compositions are shown in Figure 6. The first endothermic peak between 50 and 150°C is due to residual water evaporation. The exothermic peak around 300°C takes is associated with the pyrolysis of synthesis residues like ammonium nitrates or ammonia. The endothermic peak around 750°C corresponds to the transformation of apatitic species into β-TCP.[24,50,51]

DTA curves allow to highlight the β-TCP → α-TCP endothermic phase transition that is visible at higher temperatures with a weak endothermic signal after 1200°C. A significant increase of the phase transition temperature is visible for the co-doped compositions compared to undoped β-TCP (1210°C) (Figure 6). Among these compositions, the Mg–Sr (2.0–2.0 mol%) doped β-TCP has the highest phase transition temperature (1395°C). As seen in Figure 6, the addition of Ag^{+} and Cu^{2+} to the Mg–Sr co-doped composition leads to a slight decrease of the phase transition temperature (1380°C) compared to Mg–Sr doping alone (1395°C). However, both co-doped samples have a much higher phase transition temperature than undoped β-TCP and above 1350°C. The strong and sharp endothermic peak around 1460°C is associated with the α-TCP → α′-TCP transition, where α′-TCP is the high-temperature phase.[24,50,51]

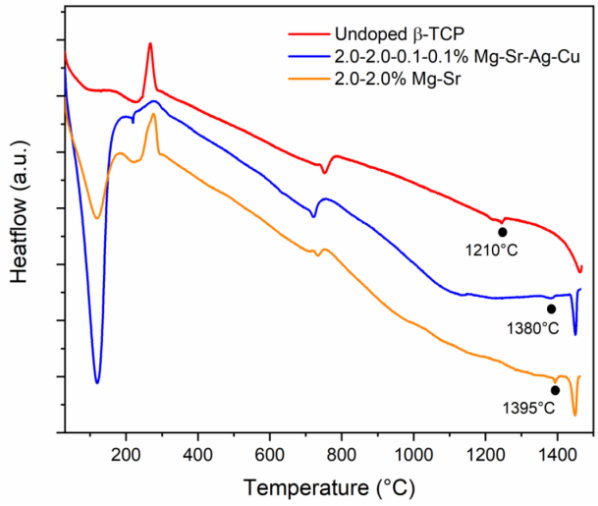

Figure 6. Differential thermal analysis (DTA) curves of undoped and co-doped β-TCP powders (1500°C, 10°C min−1 heating and cooling). Black dots represent the endothermic β–α transition.

3.3 Sintering of co-doped β-TCP pellets

Dilatometric results of casted pellets for undoped and co-doped β-TCP are presented in Figure 7. Dilatometry is mainly used to complete the DTA data about the β → α transition temperature observed for the different compositions. Indeed, the volumetric expansion associated with the β → α transition is visible in dilatometric curves.[24,28,51] Concerning the undoped β-TCP, the dilatation associated with the β → α transition occurs around 1215°C, only 5° above the temperature observed for the β → α transition in the associated DTA curve. For the co-doped compositions, the same trends are observed in dilatometric and DTA analyses with the highest phase transition temperature observed for the Mg–Sr (2.0%–2.0%) doped β-TCP (1380°C in dilatometry and 1395°C in DTA) and a slight decrease of the transition temperature with the presence of Ag^{+} and Cu^{2+} (1365°C in dilatometry and 1380°C in DTA). Moreover, dilatometric curves show the benefits of the dopants with both co-doped compositions exhibiting higher shrinkage than the undoped β-TCP. Indeed, the latter exhibits a shrinkage of only 2% until the densification is stopped by the volumetric expansion associated with the β → α transition. However, shrinkages of around 8% and 10% are observed for the Mg–Sr (2.0%–2.0%) and the Mg–Sr–Ag–Cu (2.0–2.0–0.1–0.1 mol%) compositions, respectively. The addition of Ag^{+} and Cu^{2+} proves to be efficient to increase the shrinkage during densification.

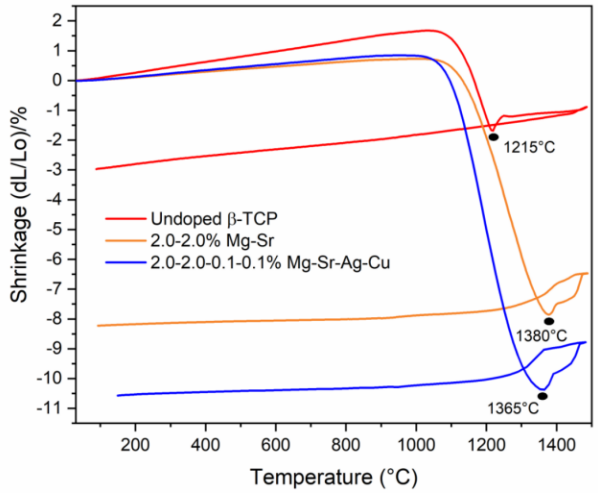

Figure 7. Dilatometric curves of undoped and co-doped β-TCP pellets (1500°C, 5°C min−1 heating and cooling). Black dots represent the β–α transition with the dilatation associated with the α-TCP formation.

The β → α transition temperatures observed with dilatometric and DTA experiments for the different compositions are compared in Table 2. Despite some differences in temperature values, the overarching trend is observed for both techniques. The observed phase transition temperatures β-TCP → α-TCP are coherent with previous works on magnesium and strontium dopings of β-TCP. Frasnelli et al.[24] and Enderle et al.[23] showed that an Mg^{2+} doping of 2.00 mol% can stabilize the β phase up to 1300°C. Concerning the co-doping with Mg^{2+} and Sr^{2+}, Tarafder et al.[21] showed a stabilization of the β-TCP up to

1250°C by adding 1 wt% SrO and 1 wt% MgO into TCP powder. Finally, a previous work of the authors emphasized the improved thermal stability of Mg–Sr (2.0–2.0 mol%) co-doped β-TCP up to 1380°C.[25]

Table 2. Observed β–α transition temperatures with differential thermal analysis (DTA) and dilatometric analyses.

Compositions	DTA: β → α (T°C)	Dilatometry: β → α (T°C)
Undoped β-TCP	≈1215	≈1215
2.0–2.0 mol% Mg–Sr	≈1395	≈1380
2.0–2.0–0.1–0.1 mol% Mg–Sr–Ag–Cu	≈1380	≈1365

XRD patterns of sintered undoped and co-doped β-TCP pellets are visible in Figure 8A (1100°C, 3 h) and in Figure 8B (1300°C, 3 h). In Figure 8A, β-TCP is the only phase present in undoped and co-doped compositions, coherent with the phase transition temperature. However, in Figure 8B, α-TCP peaks appear in the undoped composition, but co-doped compositions are still only composed of β-TCP. It appears that the phase stabilization of the β phase by the dopants is achieved up to 1300°C for these two co-doped compositions (Mg–Sr [2.0–2.0 mol%] and Mg–Sr–Ag–Cu [2.0–2.0–0.1–0.1 mol%]) in these sintering conditions. Thus, XRD results confirmed the improved thermal stability of co-doped β-TCP observed with both DTA and dilatometry curves.

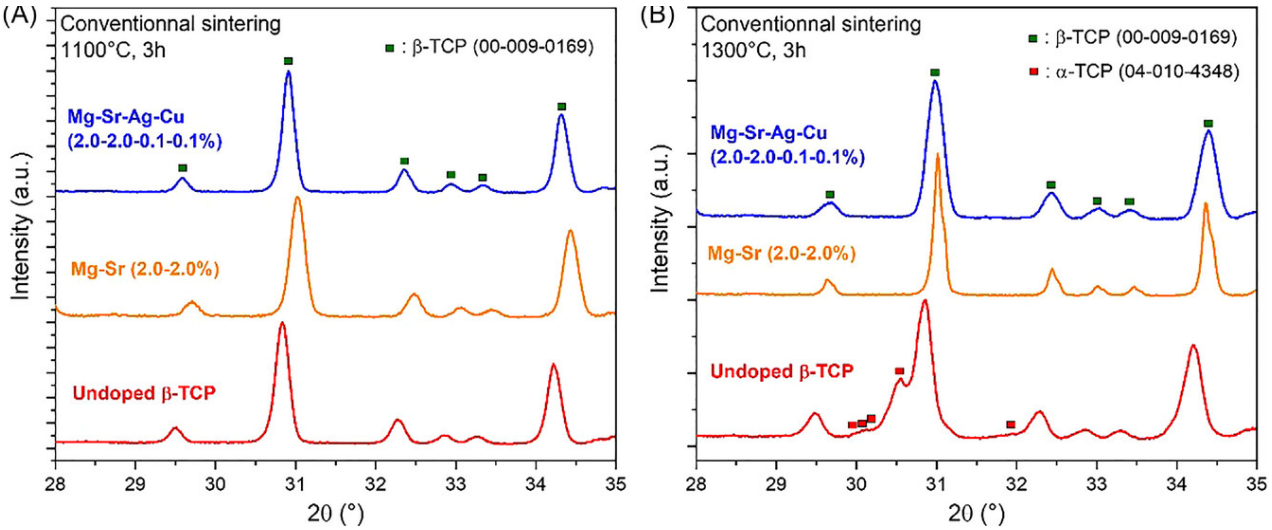

Figure 8. X-ray diffraction (XRD) patterns of sintered undoped and co-doped β-TCP pellets at (A) 1100°C for 3 h and (B) 1300°C for 3 h.

Relative densities for undoped β-TCP and two co-doped compositions are compared for both sintering temperatures (1100 and 1300°C) in Table 3.

Table 3.Relative densities of sintered pellets (3 h at 1100 and 1300°C) for undoped and co-doped β-TCP.

Composition	Relative density (%)	
	1100°C, 3 h	1300°C, 3 h
Undoped β-TCP	96.0 ± 0.3	92.8 ± 0.4
2.0–2.0 mol% Mg–Sr	97.9 ± 0.2	98.9 ± 0.2
2.0–2.0–0.1–0.1 mol% Mg–Sr–Ag–Cu	98.3 ± 0.1	99.2 ± 0.2

Densities are clearly improved with the presence of dopants, especially with sintering at 1300°C. Undoped β-TCP undergoes a drop of density from 96.0% to 92.8% between 1100 and 1300°C associated with the β → α transition. On the other hand, the corresponding densities are improved for the co-doped compositions with a sintering treatment at 1300°C compared to 1100°C. Therefore, the β-TCP phase stabilization by doping has a clear benefit on the densification allowing the use of higher sintering

temperatures. Moreover, the presence of Ag^{+} and Cu^{2+} creates a slight increase in density values compared to the Mg–Sr (2.0–2.0 mol%) composition.

As compared to some previous works on the sintering of β-TCP, the densities obtained in this work are quite high. According to Champion,[13] the highest densities achieved for β-TCP ceramic parts were in the range of 99%–99.8% R.D, where additives and hot pressing were used to improve the density. For example, Destainville et al.[52] performed hot pressing experiments (dwell of 30 min under a pressure of 20 MPa) to get pure 99.7% dense β-TCP at temperatures from 1050 to 1100°C. Douard et al.[53] used pressureless sintering (1100°C, 2 h) with the addition of silicon to get 99.8% dense β-TCP and an amorphous silicon-rich phase β-TCP. In this present work, it was possible to produce pure 99.2% dense β-TCP pellets with the addition of Mg^{2+}, Sr^{2+}, Ag^{+}, and Cu^{2+} with only pressureless sintering.

3.3.1 Microstructure

Microstructures obtained after sintering for 3 h at 1100°C are compared in Figure 9 and in Table 4 with the corresponding average grain sizes. A clear decrease of the grain size is visible with the incorporation of dopants, especially for the Mg–Sr–Ag–Cu (2.0–2.0–0.1–0.1 mol%) composition. This means the presence of Ag^{+} and Cu^{2+} cations is beneficial to limit the grain growth during the sintering process. Moreover, in addition to the reduction of grain size, the presence of dopants also allows a more homogenous grain size distribution as can be seen by the smaller standard deviation compared to undoped β-TCP. It has already been reported in the literature that dopants like Mg^{2+} and Sr^{2+} could inhibit the grain growth leading to finer microstructures.[21,25,31,49,54-56] The preservation of small grains is usually very beneficial for mechanical properties.

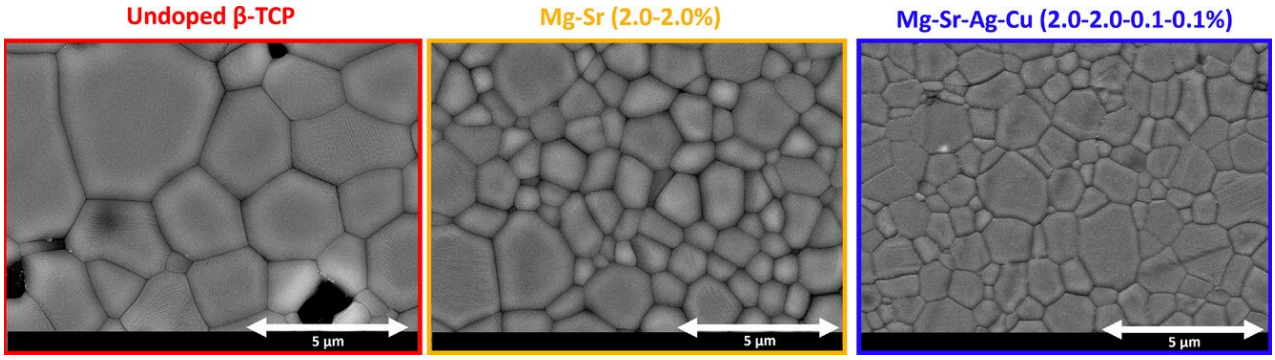

Figure 9. Micrographs of undoped and co-doped β-TCP pellets sintered at 1100°C during 3 h.

Table 4. Grain sizes of undoped and co-doped β-TCP pellets sintered at 1100°C during 3 h.

	Grain size (µm)
Compositions	**1100°C, 3 h**
Undoped β-TCP	2.87 ± 1.68
Mg–Sr (2.0–2.0 mol%)	1.64 ± 0.81
Mg–Sr–Ag–Cu (2.0–2.0–0.1–0.1 mol%)	1.28 ± 0.47

3.3.2 Mechanical properties

Vickers hardness and elastic modulus values of undoped and co-doped β-TCP (Mg–Sr [2.0–2.0 mol%] and Mg–Sr–Ag–Cu [2.0–2.0–0.1–0.1% mol]) pellets sintered at 1100°C during 3 h are reported in Figure 10.

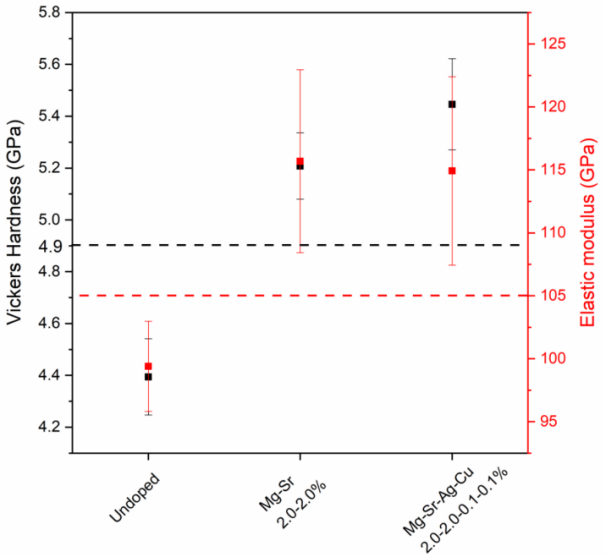

Figure 10. Vickers hardness and elastic modulus moduli of undoped and co-doped β-TCP sintered pellets (1100°C, 3 h). The dotted lines represent values obtained by Boilet et al., 2013[16] (black: Vickers hardness; red: elastic modulus).

A clear beneficial effect of doping on the Vickers hardness and elastic modulus is visible because the two co-doped compositions (Mg–Sr [2.0–2.0 mol%] and Mg–Sr–Ag–Cu [2.0–2.0–0.1–0.1 mol%] have higher values than undoped β-TCP. An improvement of around 1 GPa is visible for the Vickers hardness and around 15 GPa for elastic modulus with the incorporation of dopants. The presence of Ag^{+} and Cu^{2+} seems, once again, to have a positive effect exhibited by a slight increase of the Vickers hardness compared to the Mg–Sr (2.0–2.0 mol%) composition. As shown in Figure 9 and Table 4, the Mg–Sr–Ag–Cu-doped composition is characterized by a smaller grain size and a narrower grain size distribution compared to the Mg–Sr-doped composition and the undoped β-TCP. These smaller grain sizes and grain size distributions are at the origin of the improved mechanical properties. Typically, the compression-related microhardness of ceramics follows the Hall–Petch relation, implying the linear dependence between the microhardness and the inverse square root of grain size grain size.[57-60] Thus, a material's strength and hardness can be increased by decreasing the average crystallite grain size. This is explained by the grain boundaries that prevent the sliding of the dislocations. Smaller grains limit the size of dislocation stacks, which affects how easily dislocations can cross grain boundaries and move from grain to grain. Higher applied stress is then required to propagate grain-to-grain dislocations and permanently deform a material, effectively increasing yield strength and hardness. [57-60]

A comparison between experimental values obtained in this study and reference values from the literature is made in Figure 10 with dotted lines. Literature values come from Boilet et al.[16] who obtained a Vickers hardness of 4.9 GPa and an elastic modulus of 105 GPa for fully dense (>99.9%) undoped β-TCP pellets using hot isostatic pressing (HIP). The values obtained in the context of this work for undoped β-TCP are slightly lower with a hardness of around 4.5 GPa and an elastic modulus close to 100 GPa. However, values obtained for the co-doped compositions are quite high without the need to go through an unconventional sintering technique like HIP, highlighting the benefits of dopants.

3.4 Cell viability evaluation and cell proliferation

Cell viability results for pellets of undoped and co-doped β-TCP after 1, 3, 6, and 10 days of cellular culture are shown in Figure 11. Because the control exhibits significant fluorescence, these tests are validated. All β-TCP compositions appear identical showing that the incorporation of dopants, even Ag^{+} and Cu^{2+}, does not induce additional toxicity for up to 10 days. Slightly better cell viability is even observed for the Mg–Sr–Ag–Cu-doped β-TCP after 10 days of cellular culture compared to the two other compositions. There is also a progressive increase in measured fluorescence with the duration of cell culture, showing promising results for longer tests.

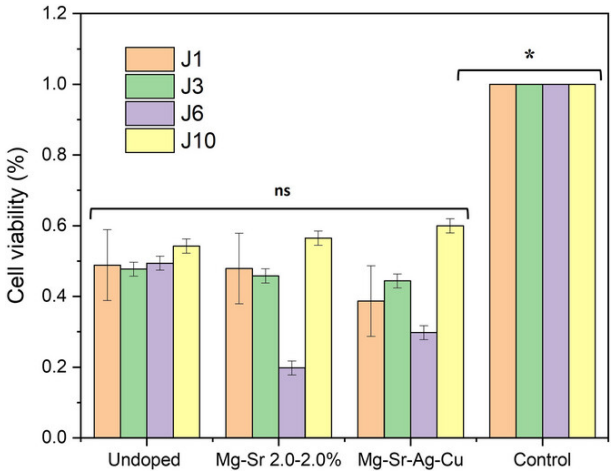

Figure 11. Cell viability (MG63 cells) results for pellets of undoped and co-doped β-TCP after 1, 3, 6 and 10 days of cellular culture obtained with the PrestoBlue test.

"" Significantly different from the tested samples ($p \leq .05$).*

Surface micrographs of sintered pellets of undoped and two compositions of co-doped β-TCP Mg–Sr (2.0–2.0 mol%) and Mg–Sr–Ag–Cu (2.0–2.0–0.1–0.1 mol%) after 6 days of cellular culture are visible in Figure 12. Cells are represented by green arrows, whereas the surfaces of pellets are indicated by red, yellow, or blue arrows.

After 6 days of cellular culture, the cell layer covers a large part of the pellet surfaces, and the cells are interconnected. The shape of these cells indicates their excellent spreading over the material. In addition, the position of their cytoplasm extensions indicated an aspiration to achieve a relationship with the neighbouring cells, which is conducive to their proliferation potential.[61] It is obvious that the cells were potentially metabolically active, as evidenced by their voluminous nature. There is a clear affinity between the β-TCP surfaces and the cells as shown by β-TCP grains/groups of grains detached from the surface and ended up on the cells or intermingled in them. Moreover, MG63 cells seem to have a certain affinity for porosity because they penetrate and colonize the pores present on the pellet surfaces (Figure 13). Comparing the undoped and co-doped β-TCP compositions, there is a minimal difference in cell behaviour on all the surfaces, indicating that with or without dopants and the presence of Ag^{+} and Cu^{2+} shows no extra sign of cytotoxicity.

Several studies showed that decreasing the grain size resulted in improved biocompatibility of potential implant materials and improved spreading of cells and their proliferation.[61-65] Among them, Veljovic et al.[61] used direct cultivation of the cells on the surface of the HAP bioceramics and showed that the HAP bioceramics with an average grain size of 130 nm stimulated the proliferation of both used cell lines much better than the HAP bioceramics with micron grain size. As explained by Bose et al.,[65] this improved the adhesion and proliferation of cells with the grain size reduction is linked to the contact angle and wettability, which are keys to cell–material interactions. Decreasing the grain size decreases the contact angle of both the water and cell media on calcium phosphate compacts. Indeed, grain boundaries increase with the decrease in grain size, and lower contact angle is a result of higher surface energy due to more grain boundaries.[65] As the Mg–Sr–Ag–Cu-doped composition is characterized by the smallest grain size (Figure 9 and Table 1), adhesion and proliferation of cells are then improved compared to the two other compositions (Mg–Sr-doped and undoped β-TCP). This hypothesis can be confirmed in Figure 11 where better cell viability is observed for the Mg–Sr–Ag–Cu doped β-TCP after 10 days of cellular culture.

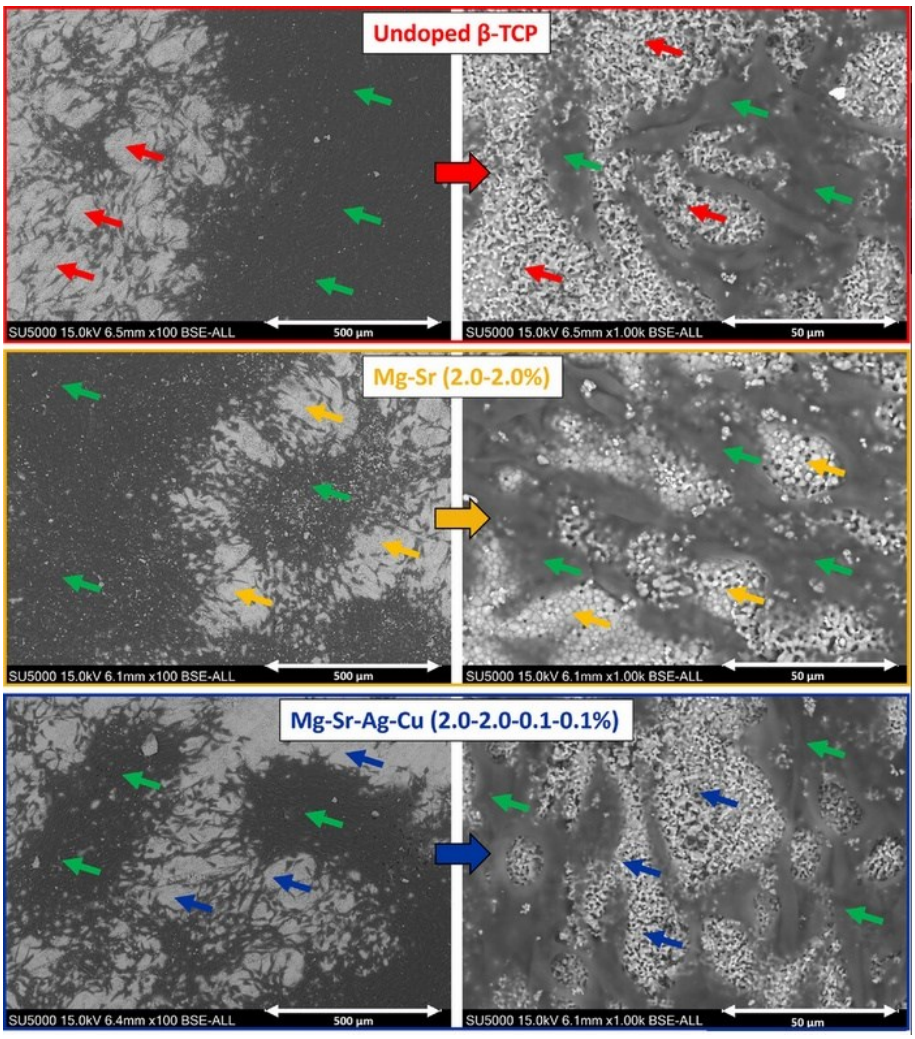

Figure 12. Surface micrographs of sintered pellets (1100°C) of undoped and two compositions of co-doped β-TCP (Mg–Sr (2.0–2.0 mol%) and (Mg–Sr–Ag–Cu [2.0–2.0–0.1–0.1 mol%]) after 6 days of cellular culture (MG63 cells). Red, yellow, and blue arrows show the surface of the pellets, whereas the green arrows show the cells spread on the pellets.

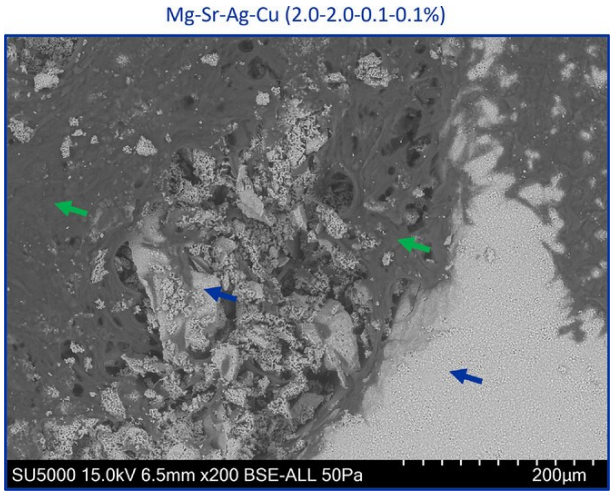

Figure 13. Surface micrographs of a sintered pellet (1100°C) of co-doped β-TCP (Mg–Sr–Ag–Cu [2.0–2.0–0.1–0.1 mol%]) after 6 days of cellular culture (MG63 cells). This micrograph shows the proliferation of MG63 cells inside the surface pores of the sample. Blue arrows show the surface of the pellets, whereas the green arrows show the cells spread on the pellets.

4. Conclusion

In this work, a co-doped composition of β-TCP was synthesized by the coprecipitation method with Mg^{2+}, Sr^{2+}, Ag^{+}, and Cu^{2+} as dopants (Mg–Sr–Ag–Cu [2.0–2.0–0.1–0.1 mol%]). XRD and IR confirmed the absence of any secondary phase. Rietveld refinement combined with ICP–AES showed a satisfactory incorporation of dopants inside the β-TCP structure.

The effects of the Ag^{+} and Cu^{2+} addition to the Mg–Sr (2.0–2.0 mol%) composition on thermal stability and mechanical and biological properties were evaluated by different techniques. A slight decrease of the phase transition temperature was observed for the Mg–Sr–Ag–Cu (2.0–2.0–0.1–0.1 mol%) composition compared to the Mg–Sr (2.0–2.0 mol%) one, but the transition temperature is still higher than 1350°C. Concerning the sintering, the presence of the four dopants allows for greater shrinkage during densification and the absence of α-TCP up to 1300°C. This led to higher densities with microstructures characterized by smaller grain sizes than Mg–Sr doped and undoped β-TCP. As a result, the Mg–Sr–Ag–Cu co-doped composition exhibits higher Vickers hardness and elastic moduli. Finally, cell proliferation assays combining fluorescence quantitative measurement and SEM observation showed no signs of cytotoxicity associated with the presence of Ag^{+} and Cu^{2+}. In addition, the reduction in grain size allows to decrease in the contact angle of both the water and cell media on Mg–Sr–Ag–Cu co-doped β-TCP pellets, leading to the adhesion and proliferation of improved cells as well as cell viability.

Thus, the use of Mg–Sr–Ag–Cu co-doped β-TCP could be very promising for biomedical applications due to the improvements of these dopants on the thermal stability and mechanical and biological properties.

Acknowledgments

The authors are grateful to the “DOC 3D Printing” project for financial support. This project has received funding from the European Union's Horizon 2020 research and innovation program under the Marie Skłodowska-Curie grant agreement no. 764935.

The authors would like to congratulate the Young Ceramists Network committee for their work to improve the networking among young ceramist researchers. The authors are also grateful to the ECERS administrative officers for their impressive work on organizing online conferences.[66]

References

1. Davies JE. Bone bonding at natural and biomaterial surfaces. Biomaterials. 2007; 28: 5058–67. https://doi.org/10.1016/j.biomaterials.2007.07.049
2. Bose S, Vahabzadeh S, Bandyopadhyay A. Bone tissue engineering using 3D printing. Mater Today. 2013; 16: 496–504. https://doi.org/10.1016/j.mattod.2013.11.017
3. Chamary S, Grenho L, Helena M, Bouchart F, Jorge F, Christophe J-C. Influence of a macroporous β-TCP structure on human mesenchymal stem cell proliferation and differentiation in vitro. Open Ceram. 2021; 7:100141. https://doi.org/10.1016/j.oceram.2021.100141
4. Chamary S, Hautcoeur D, Hornez J-C, Leriche A, Cambier F. Bio-inspired hydroxyapatite dual core-shell structure for bone substitutes. J Eur Ceram Soc. 2017; 37: 5321–7. https://doi.org/10.1016/j.jeurceramsoc.2017.05.043
5. Meurice E, Bouchart F, Hornez J-C, Leriche A, Hautcoeur D, Lardot V, et al. Osteoblastic cells colonization inside beta-TCP macroporous structures obtained by ice-templating. J Eur Ceram Soc. 2015; 36: 2895–901. https://doi.org/10.1016/j.jeurceramsoc.2015.10.030
6. Baldwin P, Li DJ, Auston DA, Mir HS, Yoon RS, Koval KJ. Autograft, allograft, and bone graft substitutes: clinical evidence and indications for use in the setting of orthopaedic trauma surgery. J Orthop Trauma. 2019; 33: 203–13. https://doi.org/10.1097/BOT.0000000000001420
7. Shin SY, Rios HF, Giannobile WV, Oh T-J. Periodontal regeneration: current therapies. Amsterdam: Elsevier Inc.; 2015. https://doi.org/10.1016/B978-0-12-397157-9.00040-0
8. Lin K, Sheikh R, Romanazzo S, Roohani I. 3D printing of bioceramic scaffolds-barriers to the clinical translation: from promise to reality, and future perspectives. Materials (Basel). 2019; 12: 2660. https://doi.org/10.3390/ma12172660

9. Habraken W, Habibovic P, Epple M, Bohner M. Calcium phosphates in biomedical applications: materials for the future? Mater Today. 2016; 19: 69–87. https://doi.org/10.1016/j.mattod.2015.10.008
10. Sohn HS, Oh JK. Review of bone graft and bone substitutes with an emphasis on fracture surgeries. Biomater Res. 2019; 23: 4–10. https://doi.org/10.1186/s40824-019-0157-y
11. Bohner M, Le Gars Santoni B, Döbelin N. β-tricalcium phosphate for bone substitution: synthesis and properties. Acta Biomater. 2020; 113: 23–41. https://doi.org/10.1016/j.actbio.2020.06.022
12. Bohner M. Resorbable biomaterials as bone graft substitutes. Mater Today. 2010; 13: 24–30. https://doi.org/10.1016/S1369-7021(10)70014-6
13. Champion E. Sintering of calcium phosphate bioceramics. Acta Biomater. 2013; 9: 5855–75. https://doi.org/10.1016/j.actbio.2012.11.029
14. Banerjee SS, Bandyopadhyay A, Bose S. Biphasic resorbable calcium phosphate ceramic for bone implants and local alendronate delivery. Adv Eng Mater. 2010; 12: 148–55. https://doi.org/10.1002/adem.200980072
15. Lu H, Zhou Y, Ma Y, Xiao L, Ji W, Zhang Y. Current application of beta-tricalcium phosphate in bone repair and its mechanism to regulate osteogenesis. Front Mater. 2021; 8: 1–16. https://doi.org/10.3389/fmats.2021.698915
16. Boilet L, Descamps M, Rguiti E, Tricoteaux A, Lu J, Petit F, et al. Processing and properties of transparent hydroxyapatite and β tricalcium phosphate obtained by HIP process. Ceram Int. 2013; 39: 283–8. https://doi.org/10.1016/j.ceramint.2012.06.023
17. Descamps M, Hornez JC, Leriche A. Effects of powder stoichiometry on the sintering of β-tricalcium phosphate. J Eur Ceram Soc. 2007; 27: 2401–6. https://doi.org/10.1016/j.jeurceramsoc.2006.09.005
18. Hudon P, Jung I-H. Critical evaluation and thermodynamic optimization of the CaO-P2O5 system. Metall Mater Trans B: Process Metall Mater Process Sci. 2015; 46: 494–522. https://doi.org/10.1007/s11663-014-0193-x
19. Renaudin G, Jallot E, Nedelec JM. Effect of strontium substitution on the composition and microstructure of sol-gel derived calcium phosphates. J Sol-Gel Sci Technol. 2009; 51: 287–94. https://doi.org/10.1007/s10971-008-1854-5
20. Banerjee SS, Tarafder S, Davies NM, Bandyopadhyay A, Bose S. Understanding the influence of MgO and SrO binary doping on the mechanical and biological properties of β-TCP ceramics. Acta Biomater. 2010; 6: 4167–74. https://doi.org/10.1016/j.actbio.2010.05.012
21. Tarafder S, Dernell WS, Bandyopadhyay A, Bose S. SrO- and MgO-doped microwave sintered 3D printed tricalcium phosphate scaffolds: mechanical properties and in vivo osteogenesis in a rabbit model. J Biomed Mater Res Part B: Appl Biomater. 2015; 103: 679–90. https://doi.org/10.1002/jbm.b.33239
22. Gomes S, Vichery C, Descamps S, Martinez H, Kaur A, Jacobs A, et al. Cu-doping of calcium phosphate bioceramics: from mechanism to the control of cytotoxicity. Acta Biomater. 2018; 65: 462–74. https://doi.org/10.1016/j.actbio.2017.10.028
23. Enderle R, Götz-Neunhoeffer F, Göbbels M, Müller FA, Greil P. Influence of magnesium doping on the phase transformation temperature of β-TCP ceramics examined by Rietveld refinement. Biomaterials. 2005; 26: 3379–84. https://doi.org/10.1016/j.biomaterials.2004.09.017
24. Frasnelli M, Sglavo VM. Effect of Mg2+ doping on beta-alpha phase transition in tricalcium phosphate (TCP) bioceramics. Acta Biomater. 2016; 33: 283–9. https://doi.org/10.1016/j.actbio.2016.01.015
25. Somers N, Jean F, Lasgorceix M, Curto H, Urruth G, Thuault A, et al. Influence of dopants on thermal stability and densification of β-tricalcium phosphate powders. Open Ceram. 2021; 7:100168. https://doi.org/10.1016/j.oceram.2021.100168
26. Tarafder S, Balla VK, Davies NM, Bandyopadhyay A, Bose S. Microwave-sintered 3D printed tricalcium phosphate scaffolds for bone tissue engineering. J Tissue Eng Regen Med. 2012; 13: 512–20. https://doi.org/10.1002/term.555
27. Obadia L. Synthèse et caractérisation des phosphates de calcium d'intérêt biologique: structure et propriétés de phosphates tricalciques β dopés au sodium, formation d'apatites non stoechiométriques par hydrolyse de phosphate dicalcique dihydraté. PhD Thesis, Université de Nantes. 2004. Retrieved from: https://archive.bu.univ-nantes.fr/pollux/show/show?id=1bb1bd7b-4e60-4f01-89aa-470d0ac37d9f

28. Cacciotti I, Bianco A. High thermally stable Mg-substituted tricalcium phosphate via precipitation. Ceram Int. 2011; 37: 127–37. https://doi.org/10.1016/j.ceramint.2010.08.023

29. Bracci B, Torricelli P, Panzavolta S, Boanini E, Giardino R, Bigi A. Effect of Mg2+, Sr2+, and Mn2+ on the chemico-physical and in vitro biological properties of calcium phosphate biomimetic coatings. J Inorg Biochem. 2009; 103: 1666–74. https://doi.org.10.1016/j.jinorgbio.2009.09.009

30. García-Páez IH, Carrodeguas RG, De Aza AH, Baudín C, Pena P. Effect of Mg and Si co-substitution on microstructure and strength of tricalcium phosphate ceramics. J Mech Behav Biomed Mater. 2014; 30: 1–15. https://doi.org/10.1016/j.jmbbm.2013.10.011

31. Veljovic D, Radovanovic Z, Dindune A, Palcevskis E, Krumina A, Petrovic R, et al. The influence of Sr and Mn incorporated ions on the properties of microwave single- and two-step sintered biphasic HAP/TCP bioceramics. J Mater Sci. 2014; 49: 6793–802. https://doi.org/10.1007/s10853-014-8380-3

32. Bellucci D, Sola A, Cacciotti I, Bartoli C, Gazzarri M, Bianco A, et al. Mg- and /or Sr-doped tricalcium phosphate/bioactive glass composites: synthesis, microstructure and biological responsiveness. Mater Sci Eng C. 2014; 42: 312–24. https://doi.org/10.1016/j.msec.2014.05.047

33. Yamasaki N, Hirao M, Nanno K, Sugiyasu K, Tamai N, Yoshikawa H, et al. A comparative assessment of synthetic ceramic bone substitutes with different composition and microstructure in rabbit femoral condyle model. J Biomed Mater Res Part B: Appl Biomater. 2009; 91: 788–98. https://doi.org/10.1002/jbm.b.31457

34. Zhang J, Wu H, He F, Wu T, Zhou L, Ye J. Concentration-dependent osteogenic and angiogenic biological performances of calcium phosphate cement modified with copper ions. Mater Sci Eng C. 2019; 99: 1199–212. https://doi.org/10.1016/j.msec.2019.02.042

35. Fadeeva IV, Gafurov MR, Kiiaeva IA, Orlinskii SB, Kuznetsova LM, Filippov YY, et al. Tricalcium phosphate ceramics doped with silver, copper, zinc, and iron (III) ions in concentrations of less than 0.5 wt.% for bone tissue regeneration. Bionanoscience. 2017; 7: 434–8. https://doi.org/10.1007/s12668-016-0386-7

36. Li G, Zhang N, Zhao S, Zhang K, Li X, Jing A, et al. Fe-doped brushite bone cements with antibacterial property. Mater Lett. 2018; 215: 27–30. https://doi.org/10.1016/j.matlet.2017.12.054

37. Laskus A, Kolmas J. Ionic substitutions in non-apatitic calcium phosphates. Int J Mol Sci. 2017; 18: 1–22. https://doi.org/10.3390/ijms18122542

38. Gokcekaya O, Ueda K, Narushima T, Ergun C. Synthesis and characterization of Ag-containing calcium phosphates with various Ca/P ratios. Mater Sci Eng C. 2015; 53: 111–9. https://doi.org/10.1016/j.msec.2015.04.025

39. Liu S, Fan C, Jin F, Zhao L, Dai K, Lu J. Preparation and antibacterial activities of porous silver-doped β-tricalcium phosphate bioceramics. Int J Appl Ceram Technol. 2015; 12: 294–9. https://doi.org/10.1111/ijac.12156

40. Fadeeva IV, Lazoryak BI, Davidova GA, Murzakhanov FF, Gabbasov BF, Petrakova NV, et al. Antibacterial and cell-friendly copper-substituted tricalcium phosphate ceramics for biomedical implant applications. Mater Sci Eng C. 2021; 129:112410. https://doi.org/10.1016/j.msec.2021.112410

41. Cummings HV. Physical and biological properties of cobalt- and copper-doped calcium phosphates as bone substitute materials (Issue NASA/TM–2018–220015 Physical). Moffett Field, California. 2018. Retrieved from https://rotorcraft.arc.nasa.gov/Publications/files/Cummings_TM-2018-220015.pdf

42. Vandecandelaere N. Élaboration et caractérisation de biomatériaux osseux innovants à base d'apatites phospho-calciques dopées. Toulouse: Université de Toulouse; 2012.

43. Bazin T, Magnaudeix A, Mayet R, Carles P, Julien I, Demourgues A, et al. Sintering and biocompatibility of copper-doped hydroxyapatite bioceramics. Ceram Int. 2021; 47: 13644–54. https://doi.org/10.1016/j.ceramint.2021.01.225

44. Doebelin N, Kleeberg R. Profex : a graphical user interface for the Rietveld refinement program BGMN. J Appl Crystallogr. 2015; 48: 1573–80. https://doi.org/10.1107/S1600576715014685

45. Abercrombie M. Estimation of nuclear population from microtome sections. Anat Rec. 1946; 94: 239–47. https://doi.org/10.1002/ar.1090940210

46. Tricoteaux A, Rguiti E, Chicot D, Boilet L, Descamps M, Leriche A, et al. Influence of porosity on the mechanical properties of microporous β-TCP bioceramics by usual and instrumented Vickers microindentation. J Eur Ceram Soc. 2011; 31: 1361–9. https://doi.org/10.1016/j.jeurceramsoc.2011.02.005

47. Hay J, Agee P, Herbert E. Continuous stiffness measurement during instrumented indentation testing. Exp Tech. 2010; 34: 86–94. https://doi.org/10.1111/j.1747-1567.2010.00618.x

48. Matsumoto N, Sato K, Yoshida K, Hashimoto K, Toda Y. Preparation and characterization of β-tricalcium phosphate co-doped with monovalent and divalent antibacterial metal ions. Acta Biomater. 2009; 5: 3157–64. https://doi.org/10.1016/j.actbio.2009.04.010

49. Kannan S, Goetz-Neunhoeffer F, Neubauer J, Pina S, Torres PMC, Ferreira JMF. Synthesis and structural characterization of strontium- and magnesium-co-substituted β-tricalcium phosphate. Acta Biomater. 2010; 6: 571–6. https://doi.org/10.1016/j.actbio.2009.08.009

50. Destainville A, Champion E, Laborde E. Synthesis, characterization and thermal behavior of apatitic tricalcium phosphate. Mater Chem Phys. 2003; 80: 269–77. https://doi.org/10.1016/S0254-0584(02)00466-2

51. Cacciotti I, Bianco A, Lombardi M, Montanaro L. Mg-substituted hydroxyapatite nanopowders: synthesis, thermal stability and sintering behaviour. J Eur Ceram Soc. 2009; 29: 2969–78. https://doi.org/10.1016/j.jeurceramsoc.2009.04.038

52. Destainville A, Rolo A, Champion E, Bernache-Assollant D. Synthesis and characterization of beta tricalcium phosphate. Key Eng Mater. 2003; 240–242: 489–92. https://doi.org/10.4028/www.scientific.net/KEM.240-242.489

53. Douard N, Detsch R, Chotard-ghodsnia R, Damia C, Deisinger U, Champion E. Processing, physico-chemical characterisation and in vitro evaluation of silicon containing β-tricalcium phosphate ceramics. Mater Sci Eng C. 2011; 31: 531–9. https://doi.org/10.1016/j.msec.2010.11.008

54. Gallo M, Le Gars Santoni B, Douillard T, Zhang F, Gremillard L, Dolder S, et al. Effect of grain orientation and magnesium doping on β-tricalcium phosphate resorption behavior. Acta Biomater. 2019; 89: 391–402. https://doi.org/10.1016/j.actbio.2019.02.045

55. Ryu HS, Hong KS, Lee JK, Kim DJ, Lee JH, Chang BS, et al. Magnesia-doped HA/β-TCP ceramics and evaluation of their biocompatibility. Biomaterials. 2004; 25: 393–401. https://doi.org/10.1016/S0142-9612(03)00538-6

56. Ryu HS, Youn HJ, Hong KS, Chang BS, Lee CK, Chung SS. An improvement in sintering property of β-tricalcium phosphate by addition of calcium pyrophosphate. Biomaterials. 2002; 23: 909–14. https://doi.org/10.1016/s0142-9612(01)00201-0

57. Sheinerman AG, Castro RHR, Yu M. A model for direct and inverse Hall-Petch relation for nanocrystalline ceramics. Mater Lett. 2020; 260:126886. https://doi.org/10.1016/j.matlet.2019.126886

58. Meyers MA, Mishra A, Benson DJ. Mechanical properties of nanocrystalline materials. Prog Mater Sci. 2006; 51: 427–556. https://doi.org/10.1016/j.pmatsci.2005.08.003

59. Wollmershauser JA, Feigelson BN, Gorzkowski EP, Ellis CT, Goswami R, Qadri SB, et al. An extended hardness limit in bulk nanoceramics. Acta Mater. 2014; 69: 9–16. https://doi.org/10.1016/j.actamat.2014.01.030

60. Hall EO. The deformation and ageing of mild steel: III discussion of results. Proc Phys Soc Sect B. 1951; 64: 747.

61. Veljovic D, Miodrag C, Kojic V, Bogdanovic G, Kojic Z, Banjac A, et al. The effect of grain size on the biocompatibility, cell – materials interface, and mechanical properties of microwave-sintered bioceramics. J Biomed Mater Res A. 2012; 100(11): 3059–70. https://doi.org/10.1002/jbm.a.34225

62. Dasgupta S, Tarafder S, Bandyopadhyay A, Bose S. Effect of grain size on mechanical, surface and biological properties of microwave sintered hydroxyapatite. Mater Sci Eng C. 2013; 33: 2846–54. https://doi.org/10.1016/j.msec.2013.03.004

63. Kim TN, Balakrishnan A, Lee BC, Kim WS, Dvorankova B, Smetana K, et al. In vitro fibroblast response to ultra fine grained titanium produced by a severe plastic deformation process. J Mater Sci: Mater Med. 2008; 19(2): 553–7. https://doi.org/10.1007/s10856-007-3204-5

64. Catledge SA, Fries MD, Vohra YK, Lace WR, Lemons JE, Woodard S, et al. Nanostructured ceramics for biomedical implants. J Nanosci Nanotechnol. 2002; 2: 293–312. https://doi.org/10.1166/jnn.2002.116

65. Bose S, Dasgupta S, Tarafder S, Bandyopadhyay A. Microwave-processed nanocrystalline hydroxyapatite: simultaneous enhancement of mechanical and biological properties. Acta Biomater. 2010; 6: 3782–90. https://doi.org/10.1016/j.actbio.2010.03.016

66. Koruza J, Klein A. Electroceramics XVII – The 2020 virtual conference experience at TU Darmstadt. Open Ceram. 2022; 6: 1–5. https://doi.org/10.1016/j.oceram.2021.100114